How Enceladus' plume depends on the crevasse wall temperature
An experimental perspective

Giordano, Fabrizio; Bourgeois, Yaël R.A.; Cazaux, Stéphanie M.; Schrijer, Ferdinand F.J.

DOI
10.1016/j.icarus.2025.116842

Publication date
2026

Document Version
Final published version

Published in
Icarus

Icarus 445 (2026) 116842

Contents lists available at ScienceDirect

Icarus

journal homepage: www.elsevier.com/locate/icarus

Research Paper

How Enceladus' plume depends on the crevasse wall temperature: An experimental perspective

Fabrizio Giordano [a], Yaël R.A. Bourgeois [a,b], Stéphanie M. Cazaux [a,b,*], Ferdinand F.J. Schrijer [a]

[a] Faculty of Aerospace Engineering, Delft University of Technology, Delft, The Netherlands
[b] Leiden Observatory, Leiden University, P.O. Box 9513, NL 2300 RA Leiden, The Netherlands

ARTICLE INFO

Keywords:
Enceladus
Plume
Experiments
Water vapour
Triple point
Heat transfer
Mach number
Nucleation
Solid fraction
Convection
Thermal radiation

ABSTRACT

In this study, plume experiments were conducted to mimic the thermodynamic conditions on Saturn's moon, Enceladus. The icy moon's subsurface ocean and cracks in the surface have been simulated using a liquid water reservoir and a narrow channel, while the low-pressure environment at Enceladus' surface was achieved with a vacuum chamber. We aimed to examine how channel temperature affected the plume's temperature, solid fraction and velocity, testing two models with differing wall temperatures: room temperature and near 0 °C. The colder setup better replicated Enceladus' plume, producing a saturated flow in which nucleation of icy particles is possible. A conservative 1.5%–3% minimum solid fraction is estimated from measurements and modelling. Pitot-tube measurements indicated velocities around 400–500 m/s at the channel outlet. Flow temperature and velocity are closely correlated with wall temperature, indicating effective heat transfer. With a plume model based on the energy conservation law, we concluded that supersonic plume velocities observed on Enceladus cannot be achieved with straight channels, *i.e.* without requiring extreme expansion ratios. Additionally, the research provides evidence of the relationship between the crevasse's expansion ratio and the temperatures of flow and crevasse walls.

1. Introduction

Since the Cassini discovery of water vapour and ice particle plume that is emitted from Enceladus' south polar region in 2005 (Porco et al., 2006), multiple studies have been carried out to characterise these ejections originating from elongated crevasses known as the "Tiger Stripes". Similar plume activity has also been suggested on other icy bodies in the Solar System, such as Jupiter's moon Europa (Goodman et al., 2004; Choukroun et al., 2020; Vorburger and Wurz, 2021) and Neptune's moon Triton (Hansen et al., 1990; Soderblom et al., 1990), highlighting the broader relevance of studying such phenomena. The most accepted plume formation theory involves liquid water vaporisation (Porco et al., 2006; Postberg et al., 2009; Ingersoll and Ewald, 2011) from a subsurface ocean lying beneath a 3–5 km thick ice shell (Hemingway et al., 2018). Cassini observations have provided valuable insights into plume characteristics: vent temperatures range between 145 K and 210 K (Spencer et al., 2006; Spencer and Nimmo, 2013; Goguen et al., 2013; Tenishev et al., 2014), ice–vapour mass ratios are estimated between 0.07 (Gao et al., 2016) and 0.7 (Kieffer et al., 2009; Ingersoll and Ewald, 2011), and the water vapour can reach supersonic velocities (Hansen et al., 2006; Tian et al., 2007; Hansen et al., 2008; Smith et al., 2010; Dong et al., 2011), with Mach numbers of some jets above 5 (Hansen et al., 2011; Perry et al., 2015; Fu et al., 2021; Portyankina et al., 2022).

From Cassini occultation data, an estimated 170 to 250 kg/s of vapour escapes from Enceladus (Hansen et al., 2006, 2011, 2017), with solid particles, nanograins and ions accounting for another estimated cumulated 40 kg/s (Kempf et al., 2018; Ingersoll and Ewald, 2011; Dong et al., 2015). The total heat flow is estimated between 3.9 and 7.7 GW south of 65 °S (Spencer et al., 2006). Multiple theoretical models have been proposed to constrain the heat and mass transfer involved in the geological activity of the moon (Matson et al., 2012; Kite and Rubin, 2016; Mitchell et al., 2024), as well as crevasses geometry and conditions of the water vapour flow (Ingersoll and Pankine, 2010; Tucker et al., 2015; Nakajima and Ingersoll, 2016; Ingersoll and Nakajima, 2016; van der Hijden et al., 2024). These models all underpin key processes happening at the water table, where liquid water turns into plume; boiling, with contributions from gas exsolution (Fifer et al., 2022) accounts for the vapour phase while nucleation as well as droplets freezing (Klenner et al., 2025) takes care of the solid phase. Crevasse widths ranging between 0.05–0.075 m have been estimated by Nakajima and Ingersoll (2016) to explain the mass flow rate observed from Cassini, while widths of 1 m are necessary to avoid

* Corresponding author at: Faculty of Aerospace Engineering, Delft University of Technology, Delft, The Netherlands.
E-mail address: s.m.cazaux@tudelft.nl (S.M. Cazaux).

https://doi.org/10.1016/j.icarus.2025.116842
Received 28 April 2025; Received in revised form 3 October 2025; Accepted 6 October 2025
Available online 17 October 2025

freezing of the liquid water surface (Ingersoll and Nakajima, 2016). Ingersoll and Pankine (2010) and Nakajima and Ingersoll (2016) found that the difference between local flow temperature and crevasse wall temperature was below 2 K. Different geometries have been studied by van der Hijden et al. (2024), pointing out the influence of nucleation onto the flow temperature and giving an estimate of the timescale of the ice cracks lifetime.

With a series of laboratory experiments, we aim to further investigate the plumes' characteristics. We have developed an experimental plume setup consisting of a water reservoir and a channel, respectively emulating the subsurface ocean of Enceladus and a crevasse in the ice crust. The setup has been placed in a vacuum chamber to achieve water triple point conditions in the reservoir and 10^{-3} bar in the chamber. In this study, we investigate the influence of the temperature of the channel walls on the flow characteristics, with a focus on the heat transfer with the flow, the solid fraction and the venting velocity. The article is organised as follows: Section 2 describes the experimental set-up and the methods used to process the laboratory measurements; Section 3 presents the results of the experiments; in Section 4, we discuss the influence of heat transfer processes on the flow conditions and estimate the solid fraction generated through nucleation; Section 5 extends our experimental findings to Enceladus' condition and discusses their implications. Section 6 outlines the conclusions of this research.

2. Experimental setup and data processing

The experiments were conducted using a plexiglass reservoir containing demineralised water to mimic the subsurface ocean and a 3D printed PLA (poly-lactic acid) channel to simulate a crevasse in the ice crust of Enceladus. For this study, we consider a circular and uniform cross-sectional area channel, with a length of 245 mm and a diameter of 5.7 mm. A sketch of the experimental setup is given in Fig. 1. The setup is placed inside a vacuum chamber, evacuated throughout the experiment by two vacuum pumps to achieve pressures below the saturation point of water vapour, causing the water to boil. The vaporised water flows through the channel, with temperature and pressure being monitored, before being expelled into the vacuum chamber. Furthermore, total pressure measurements are performed at the vent of the channel. A splash screen is installed at the channel inlet to prevent liquid water droplets, generated by bursting bubbles on the water surface, from entering the channel and compromising the measurements. The experiment ends when the pumps are stopped and the chamber is re-pressurised. Additional information on the vacuum chamber and measuring equipment is included in Appendix A.

The first series of experiments was conducted without any control over the channel temperature (or wall temperature), which was at room temperature at the beginning of each experiment. For simplicity, this experimental setup is designated as the *warm* setup. A subsequent set of experiments is performed with an ice block encased around the outer surface of the channel, cooling the channel walls throughout the experiment. This channel configuration is denoted as the *frozen* setup. Melting of ice before starting the experiment ensured that the internal surface of the channel was at approximately 0 °C. However, as the vacuum chamber reached low pressures, sublimation of the ice cooled both the ice and the plastic channel. Temperature measurements were taken at several points on the internal surface of the channel in the absence of gas flow and in vacuum conditions. Temperatures between 0 and −5 °C were recorded across the channel, showing no noticeable changes over time. Since no gas was flowing, the measured temperatures are considered a good indication of the actual channel temperature.

Temperature and pressure are measured in the reservoir and along the channel as indicated in Fig. 1. T-type thermocouples have been employed to measure the temperature, with an estimated uncertainty of 2 °C, and differential pressure sensors to measure the pressure, with an uncertainty of 0.1–0.3 mbar. The thermocouples were positioned with their tips aligned to the channel axis. In contrast, the pressure sensors were placed in a thermally stable area of the vacuum chamber to ensure reliable measurements and were connected to tubes that sampled the pressure along the channel wall.

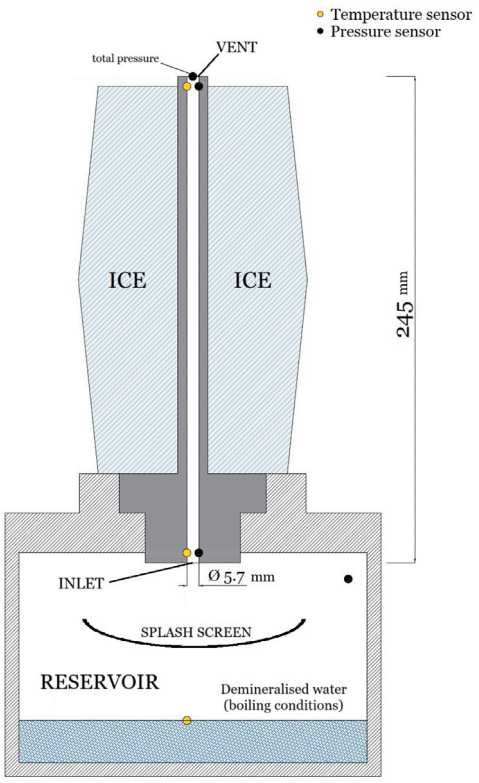

Fig. 1. Schematic of the experimental setup. The channel is mounted on top of a plexiglass reservoir containing demineralised water. The setup is placed inside a vacuum chamber.

The acquired data is used to derive other flow parameters. The first is the *saturation degree*, providing an indication of how close the flow is to the saturation condition and defined as in Eq. (1). In this equation, p_{flow} is the flow pressure and $p_{eq}(T_{flow})$ is the *equilibrium pressure*, or *saturated vapour pressure*, dependent on the flow temperature and calculated with the Antoine relation[1] in Eq. (2).

$$S = \frac{p_{flow}}{p_{eq}(T_{flow})} \tag{1}$$

$$p_{eq} = 10^{\mathcal{A} - \frac{\mathcal{B}}{\mathcal{C}+T_{flow}}} \tag{2}$$

In this study, the saturation degree is used as an indicator of possible icy grain formation within the water vapour flow, known as *nucleation*. Since demineralised water is used, the vapour is free from impurities and particles that could trigger heterogeneous nucleation. Therefore, only homogeneous nucleation is expected to occur in these conditions (Viisanen et al., 1997).

The Mach number (M) at the vent is obtained from static pressure (p) and total pressure measurements (p_0) using Eq. (3) (see derivations in Appendix B), assuming the flow locally isentropic. The heat capacity ratio (γ) of water vapour is equal to 4/3, assuming ideal gas conditions.

$$M = \sqrt{\frac{2}{\gamma - 1} \cdot \left[\left(\frac{p_0}{p} \right)^{\frac{\gamma-1}{\gamma}} - 1 \right]} \tag{3}$$

[1] Coefficients $\mathcal{A}$, $\mathcal{B}$ and $\mathcal{C}$ have been calculated by the *NIST*, based on the study of Stull (1947): https://webbook.nist.gov/cgi/cbook.cgi?ID=C7732185&Mask=4&Type=ANTOINE&Plot=on.

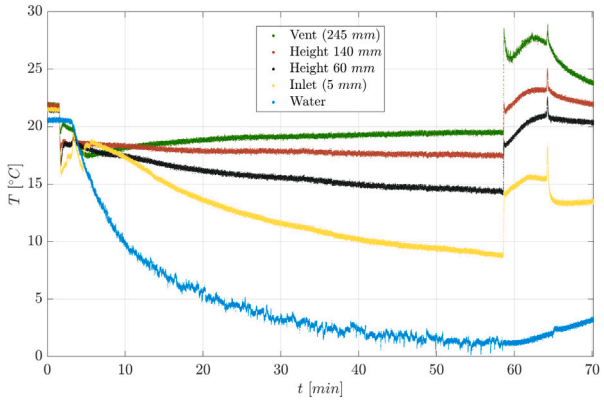

(a) Temperature of liquid water/water vapour during an experiment in warm configuration.

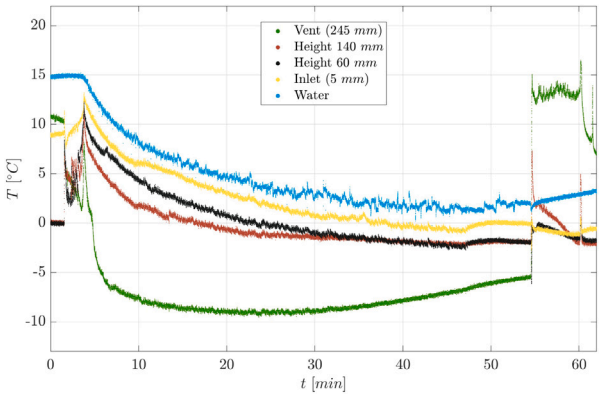

(b) Temperature of liquid water/water vapour during an experiment in frozen configuration.

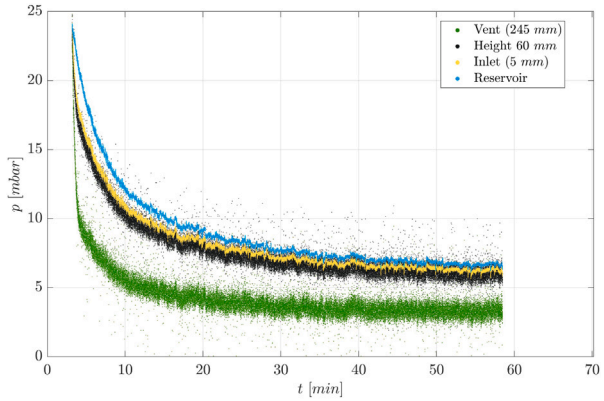

(c) Pressure of water vapour during an experiment in warm configuration.

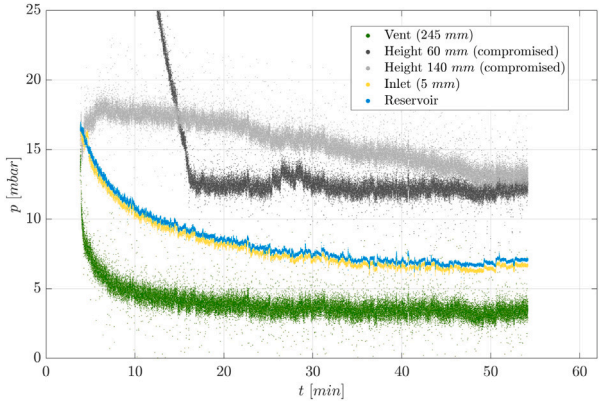

(d) Pressure of water vapour during an experiment in frozen configuration.

Fig. 2. Typical water (vapour) temperature and pressure measured during plumes-analogue experiments (warm configuration on the left, frozen configuration on the right). The pressure was measured from the moment the water in the reservoir started boiling, until the vacuum pumps were deactivated. (For interpretation of the references to colour in this figure legend, the reader is referred to the web version of this article.)

The velocity at the vent (V_{vent}) is determined by multiplying the Mach number obtained with Eq. (3) by the speed of sound c_s:

$$c_{s,vent} = \sqrt{\gamma R / \mathcal{M}_{H_2O} T_{vent}} \tag{4}$$

where γ is the heat capacity ratio, equal to 4/3 assuming ideal gas, R is the universal gas constant, $\mathcal{M}_{H_2O}$ represents the molar mass of water and T_{vent} is the temperature of the water vapour flow measured at the vent.

3. Measurements of flow conditions

In this section, we show the results obtained with the warm model and frozen model and describe the differences between them. Flow temperature and pressure are measured along the channel and used to calculate saturation degree (S) and Mach number (M).

3.1. Temperature and pressure profiles

The typical temperature of the liquid water and water vapour along the channel during warm and frozen configuration experiments is shown in Figs. 2(a) and 2(b) respectively. The figures also show the main events during the depressurisation cycle, namely when the vacuum pumps are activated (around 1–2 min from the start), when the liquid water reservoir reaches boiling conditions (between 3–5 min) and when the chamber is repressurised (between 50 and 60 min).

For the same experiments, the pressure measured in the reservoir and along the channel is displayed in Figs. 2(c) and 2(d). The data collection began once the reservoir reached boiling conditions and continued until the temperatures and pressures had stabilised, at which point the vacuum pumps were deactivated. The pressure at the vent was measured to be approximately 3.5 mbar, consistent with the numerical values reported by van der Hijden et al. (2024). As visible from Fig. 2(d), the pressure measurements at 60 and 140 mm of channel height for frozen model experiments were unreasonably high, changing very slowly compared to the depressurisation of the chamber and reservoir or showing sudden jumps when not expected. We hypothesise that during the freezing process, the ice expanded, clogging the plastic tubes used to probe the pressure inside the channel and, consequently, compromising the measurements.

3.2. Reservoir conditions

Regardless of the experiment duration, triple point conditions and water freezing were not observed in the reservoir at any moment, although the system appeared to approach these conditions. Each experiment was stopped once the pressure and temperature in the reservoir stabilised, showing no noticeable changes over time. The stable reservoir conditions were approximately 7 mbar and 0–3 °C, independent of the experimental setup temperature and reservoir initial conditions. The chamber pressure under these conditions was consistently around 3–3.5 mbar.

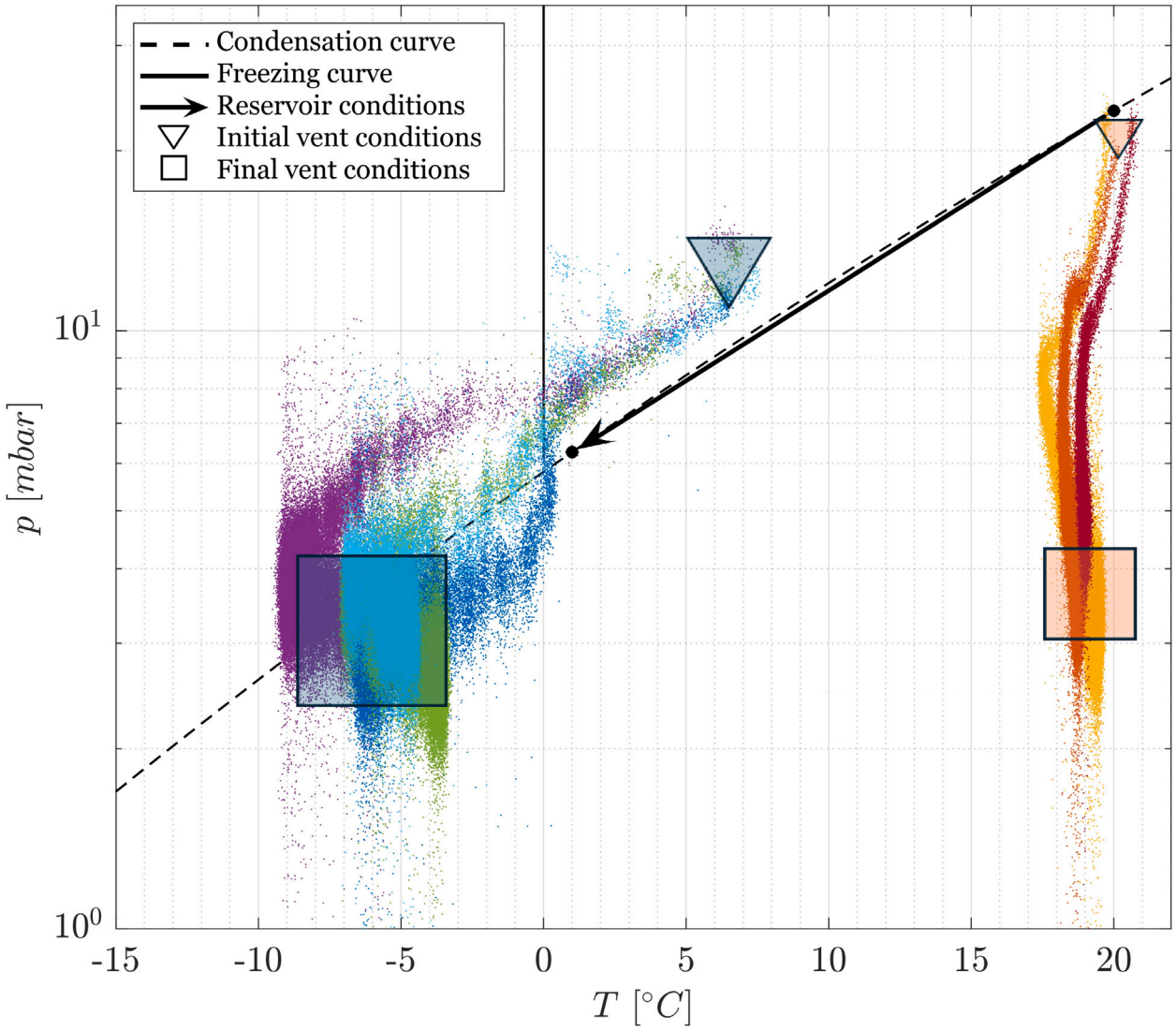

Fig. 3. Pressure–temperature conditions of the water vapour flow measured at the vent of 3 experiments in warm configuration and 4 experiments in frozen configuration. The colours follow the notation in Table 1. Temperature and pressure are measured with relative sensors positioned along the channel. The black arrow indicates the evolution of reservoir conditions. Triangle and square symbols mark the initial and final flow conditions at the vent, respectively. (For interpretation of the references to colour in this figure legend, the reader is referred to the web version of this article.)

One possible reason why triple point conditions and water freezing did not occur in the reservoir is the restriction of water vapour outflow caused by the channel, combined with heat radiated from the surrounding environment. The geometrical constriction may have generated a back-pressure in the reservoir, inhibiting the water vapourisation process. Additionally, the slow heat loss from the reservoir may have been balanced by the heat absorbed from the vacuum chamber environment (at approximately 15 °C) by the liquid water. Additional experiments with different channel diameters have been performed to investigate this hypothesis. However, the results will be part of a future publication.

3.3. Temperature–pressure conditions at the vent

The temperature and pressure conditions measured at the channel vent are shown in Fig. 3. Data were acquired at 20 Hz, starting when the water in the reservoir reached boiling conditions, marked by triangle symbols in the figure. Acquisition was stopped once stable flow conditions were achieved, indicated by shaded squares. A summary of the results and uncertainties associated with each experiment is reported in Table 1.

For Enceladean conditions, theoretical models predict a decrease in gas temperature along the channel as a consequence of the rapid decrease in flow pressure, ultimately reaching saturation conditions (Schmidt et al., 2008; Yeoh et al., 2015; Nakajima and Ingersoll, 2016). While the vent conditions measured in the frozen experimental setup are consistent with the theory, the flow at the vent of the warmer setup immediately diverges from the saturation conditions, maintaining a flow temperature between 17 and 20 °C throughout the experiment. In both warm and cold models, the flow stabilises at a temperature similar to the wall temperature of the model while the pressure conditions in the reservoir and the chamber are nearly identical. Therefore, the variation in the temperature of the channel wall must be the primary cause of the difference in the observed flow temperature at the vent.

The venting temperatures of the warm model, higher than the water temperature, suggest a transfer of heat from the warmer walls to the flowing gas. This phenomenon likely involves a significant contribution from convection and thermal radiation, both of which are sensitive to wall temperature.

Table 1
Summary of experimental results. A number and a distinct colour identify each experiment, consistent across Figs. 3, 4, 5, 6, and 7. For each experiment, the configuration type (warm or frozen), the duration of the experiment Δt (in minutes) and the saturation degree S under stable conditions are reported. Estimated Mach numbers M in stable flow conditions are also provided for experiments where velocity measurements were not compromised.

Exp.	T_{wall}	Δt [min]	S	M
1	Warm	55	0.15 ± 0.02	0.63 ± 0.18
2	Warm	61	0.17 ± 0.03	–
3	Warm	17	0.20 ± 0.03	–
4	Frozen	28	0.77 ± 0.14	0.84 ± 0.14
5	Frozen	40	0.78 ± 0.15	0.94 ± 0.14
6	Frozen	47	0.58 ± 0.11	0.86 ± 0.17
7	Frozen	50	0.90 ± 0.17	–

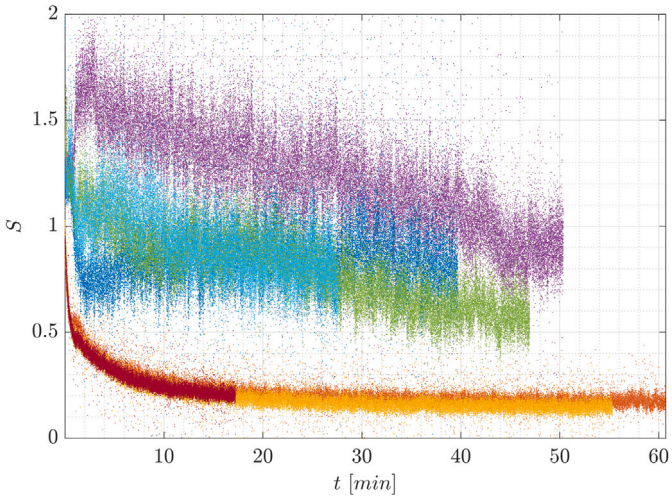

Fig. 4. Saturation degree computed with pressure and temperature measurements at the vent of the channel using Eq. (1). The colour scheme from Table 1 is used. (For interpretation of the references to colour in this figure legend, the reader is referred to the web version of this article.)

3.4. Observations of phase change

On a theoretical level, the decrease in flow pressure along the channel causes the flow temperature (T_{flow}) to decrease, consequently decreasing p_{eq} (see Eq. (2)) and increasing S (see Eq. (1)). In an isentropic flow, no heat is exchanged with the walls and no phase change occurs, leading to a very high value of saturation degree ($S \gg 1$). In reality, S values above 1 are not sustainable, since vapour at a pressure above the saturated pressure (p_{eq}) tends to change phase: when $p_{flow} > p_{eq}$, water vapour transitions to solid phase, forming ice nuclei that grow into larger particles through condensation. Alternatively, ice particles can also form from the freezing of liquid water droplets, which are generated by boiling water and entrained by the upward-moving flow. In this work, both processes are collectively referred to as *nucleation*. Nucleation releases heat to the flow and increases its temperature, re-establishing a saturation degree around 1.

For the warm model, Fig. 4 shows that the flow has a saturation degree well below 1, indicating that the water vapour pressure is lower than p_{eq}. This result suggests that the heat exchanged between the flow and the walls plays an important role, increasing the flow temperature (T_{flow}) and, with it, the saturated vapour pressure (p_{eq}).

On the other hand, Fig. 4 shows that the water vapour flow in the frozen model has a higher saturation level. The colder model temperature allows the flow temperature to decrease while travelling along the channel, resulting in higher S than in the warm model. Since phase change prevents the flow from becoming super-saturated ($S \gg 1$), the values of S close to 1, displayed in Fig. 4, suggest that nucleation is significantly more likely to occur in the frozen experimental setup compared to the warm one.

The decrease in saturation degree with time displayed in Fig. 4 can be linked to a change in the thermal condition of the system. Specifically, the reservoir water temperature decreases due to the evaporation process, leading to a corresponding decrease in flow temperature. Once the water reaches a constant temperature, between 0–3 °C, the saturation degree also stabilises.

It remains unclear whether the higher saturation degree observed at the beginning of each experiment indicates increased nucleation. Interpreting this initial phase is challenging due to its transitional nature and the influence of multiple factors. One such factor is condensation from saturated air on the reservoir walls during the evacuation of the vacuum chamber, which likely disturbs the measurements in this phase.

Water droplets were also observed on the channel walls at the end of the experiments, when the chamber was repressurised and the model could be closely inspected. The frozen setup exhibited significant condensation, given the colder surfaces where water vapour is more likely to deposit. In several instances, this condensation resulted in ice particle formation on the channel walls and subsequent clogging, which disrupted multiple experimental runs of the frozen setup.

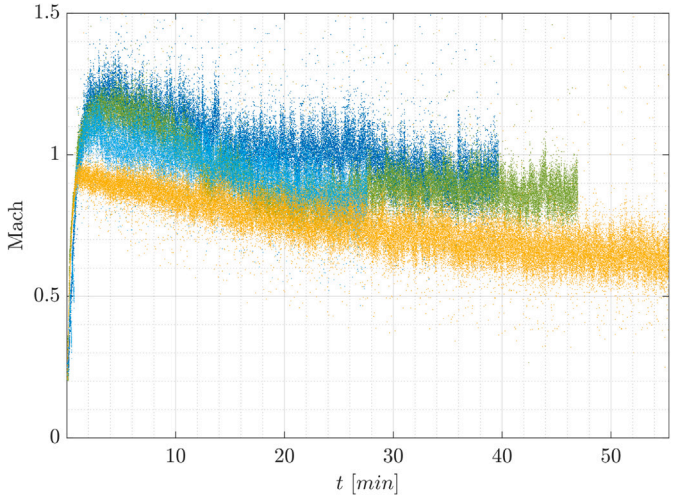

Fig. 5. Mach number computed from total and static pressure measurements at the channel vent, using the isentropic relation in Eq. (3). The colour scheme from Table 1 is used. (For interpretation of the references to colour in this figure legend, the reader is referred to the web version of this article.)

3.5. Mach number measurements

The Mach number of the flow at the vent is determined using Eq. (3). Experiments 2, 3, and 7 were excluded from the analysis due to unreliable total pressure measurements, caused by water droplets clogging the Pitot-tube pressure probe. The results displayed in Fig. 5 show a clear discrepancy between the two setups, with the colder one exhibiting higher velocities, which implies higher Mach numbers. Since the frozen setup and warm setup present similar reservoir conditions and vacuum chamber pressures, we would expect similar velocities too. Therefore, the disparity can be attributed to thermal effects occurring inside the channel, as we already inferred for the temperature variations at the vent.

Similar to the saturation degree, the Mach number also shows changes with time, likely due to changes in reservoir conditions. Again,

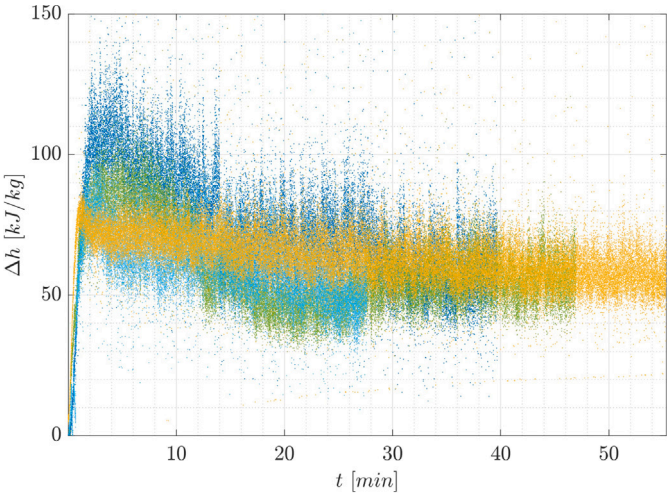

Fig. 6. Enthalpy difference between vent and inlet computed with Eq. (5). Velocity at the vent has been derived from the Mach number measurements, multiplied by the speed of sound under the ideal gas assumption. The colour scheme from Table 1 is used. (For interpretation of the references to colour in this figure legend, the reader is referred to the web version of this article.)

we observe that this variability almost disappears at the end of the experiments, when the reservoir and water vapour flow are in stable conditions. In these steady conditions, Mach numbers range between 0.8–1 in the frozen setup and 0.6–0.7 in the warm setup, corresponding to estimated velocities of approximately 320–500 m/s and 260–390 m/s, respectively, calculated using Eq. (4).

4. Heat exchange between flow and models

Results presented in Section 3 are here used to investigate and quantify the influence of heat transfer between the flow and the channel walls and to estimate the solid fraction for frozen model experiments.

4.1. Vent enthalpy difference

According to the energy conservation equation in a steady flow, the energy of water vapour at the *inlet* of the channel (see Fig. 1) should match the energy at the vent, as expressed in Eq. (5). Using this equation, we calculate the enthalpy excess at the vent (Δh_{vent}) due to heat transfer processes and nucleation throughout the plume experiments.

$$c_{p,inlet}T_{inlet} = c_{p,vent}T_{vent} + \frac{V_{vent}^2}{2} - \Delta h_{vent} \tag{5}$$

In Eq. (5), c_p is the specific heat capacity of water vapour. The inlet enthalpy does not include the kinetic energy term, since the velocity in this location is assumed ~0. The velocity at the vent (V_{vent}) is determined multiplying the Mach number obtained in Section 3.5 by the speed of sound ($c_{s,vent} = \sqrt{\gamma R_{sp} T_{vent}}$), where $R_{sp} = R/\mathcal{M}$, and $\mathcal{M}$ represents the molar mass of H_2O.

The results reported in Fig. 6 denote a peak in Δh_{vent} in the first minutes of the experiments which are attributed to large variations in thermodynamic conditions in the reservoir. In this initial phase, the frozen model presents values nearly double those of the warm model, despite its velocity being only slightly higher. A possible interpretation is that the temperature difference between water vapour flow and the frozen model is highest at the beginning of the experiment, when water is above 10 °C, resulting in larger thermal effects inside the channel. However, in stable conditions, Fig. 6 shows Δh_{vent} values similar for both models.

4.2. Heat exchange between flow and model

Values of Δh (J/kg) found in Section 4.1 are here used to estimate the amount of heat absorbed by the flow (W) from the channel walls. As expressed in Eq. (6), we consider the heat flux through convection ($\dot{Q}_{conv}$) and nucleation ($\dot{Q}_{nucl}$) as main contributors to the total enthalpy difference (Δh_{vent}) observed at the vent. The mass flow rate of water vapour is indicated as $\dot{m}_{flow}$.

$$\dot{Q}_{tot} = \dot{Q}_{conv} + \dot{Q}_{nucl} + \dot{Q}_{other} = \dot{m}_{flow}\Delta h_{vent} \tag{6}$$

Among the other energy sources grouped in $\dot{Q}_{other}$ in Eq. (6), radiative heat transfer is included. However, due to the gaseous and rarefied nature of the flow, we assume that the contribution of radiative heat transfer is negligible. Moreover, as discussed in Section 3, phase change can be disregarded in the warm model, given the low saturation degree.

Convection, described by Eq. (7), is likely the dominant mode of heat transfer in this system. In the equation, h_{conv} represents the convective heat transfer coefficient, A is the surface area of the channel exposed to the flow and $(T_{wall} - T_{flow})$ is the temperature difference between the channel walls and the water vapour flow.

$$\dot{Q}_{conv} = h_{conv}A\left(T_{wall} - T_{flow}\right) \tag{7}$$

An estimated value for h_{conv} is approximately 15–20 W/m^2 K, as calculated in Appendix C.

To obtain an indicative $\dot{Q}_{tot}$ value exchanged with the flow inside the channel, we substituted the enthalpy calculated with Eq. (5) in Eq. (6) and an estimate of the mass flow rate. Appendix D provides different methods to obtain this value. Calculations show that $\dot{m}_{flow}$ is around 10^{-5} kg/s under stable conditions. By substituting $\dot{m}_{flow}$ and Δh_{vent} into Eq. (6), we obtain a total power around 0.5–1 W.

4.3. Solid fraction

While nucleation is considered negligible in the warm model, it can significantly impact the flow inside the frozen model, as shown in Section 3.4. This section aims to quantify the solid fraction in the flow of the frozen model produced through nucleation, defined as the mass of ice particles nucleating ($\dot{m}_{nucl}$) with respect to the total mass flow ($\dot{m}_{flow}$).

Eq. (8) describes the heat released through nucleation, which is directly proportional to $\dot{m}_{nucl}$ and L_v. The latter is either the latent heat of vaporisation or sublimation of water, depending on whether the flow temperature is above or below 273.15 K. By definition, $\dot{m}_{nucl}$ is equal to the solid fraction f of the flow times the mass flow rate $\dot{m}_{flow}$. In the regime where the difference $T_{wall} - T_{flow}$ is negligible, nucleation is considered the only process contributing to the total Δh. Therefore, Eq. (6) can be simplified to Eq. (9). The solid fraction is subsequently computed by combining the two expressions of $\dot{Q}_{nucl}$, resulting in Eq. (10).

$$\dot{Q}_{nucl} = \dot{m}_{nucl}L_v = f\dot{m}_{flow}L_v \tag{8}$$

$$\dot{Q}_{nucl} = \dot{m}_{flow}\Delta h_{vent} \tag{9}$$

$$f = \frac{\Delta h_{vent}}{L_v} \tag{10}$$

Values of solid fraction needed to account for the excess enthalpy at the vent observed in Fig. 6 have been plotted for 3 frozen model experiments in Fig. 7, showing f values between 1.5% and 3%, with the highest values observed in the first 10–15 min of each experiment. The decrease in solid fraction with time agrees with the saturation degree decrease observed in Fig. 4.

It is worth noting that including the effect of convection and thermal radiation cooling or heating would influence these estimates and Eq. (9) does not exactly hold anymore. In the first phase of the frozen model experiments, the flow is cooled by the walls ($T_{wall} < T_{flow}$), with $\dot{Q}_{conv}$ and $\dot{Q}_{rad}$ assuming negative values. Therefore, under these conditions, nucleation is underestimated (see Eq. (6)) and the results in Fig. 7 can be regarded as conservative estimates representing the minimum solid fraction achieved in our experiments.

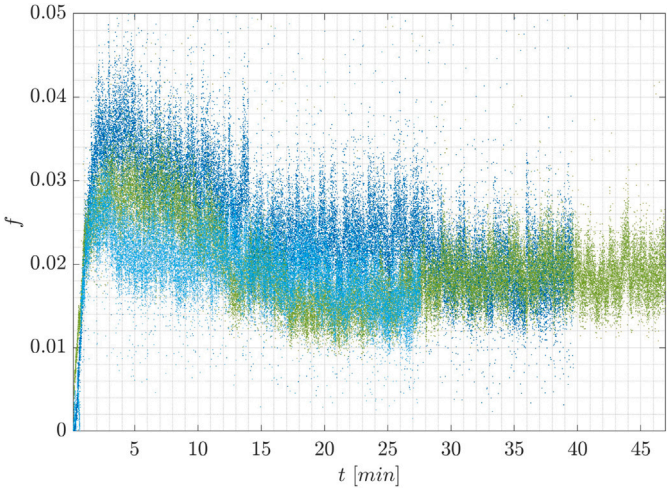

Fig. 7. Solid fraction at the vent of the frozen model computed from enthalpy difference at the vent (Δh_{vent}) using Eq. (8). The colour scheme from Table 1 is used. (For interpretation of the references to colour in this figure legend, the reader is referred to the web version of this article.)

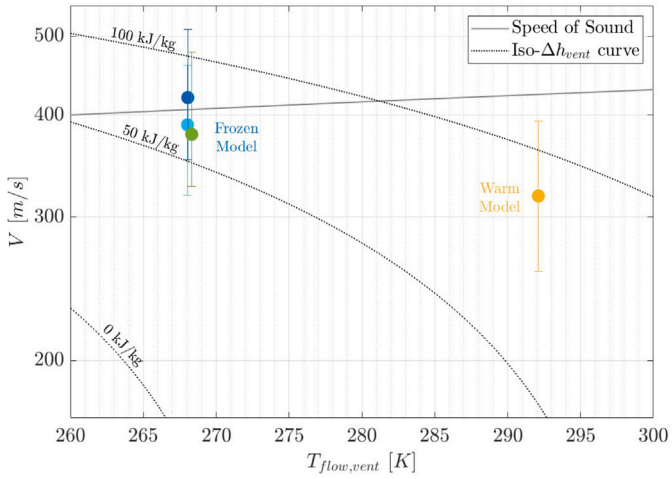

Fig. 8. Average flow velocity at the vent in the frozen model. Black dotted lines show indicative velocities for different vent flow temperatures ($T_{flow,vent}$), estimated through the energy conservation equation (Eq. (5)) for different values of Δh_{vent}. (For interpretation of the references to colour in this figure legend, the reader is referred to the web version of this article.)

5. Experimental results extended to Enceladus's conditions

In this section, the experimental results are compared with the plume characteristics inferred from Cassini observations. The solid fractions are compared with estimates from the Imaging Science Subsystem (*ISS*) and the Ultraviolet Imaging Spectrograph (*UVIS*) data (Kieffer et al., 2009; Ingersoll and Ewald, 2011), from the Plasma Wave Spectrometer (*RPWS*), the Cassini Plasma Spectrometer (*CAPS*), and the Ion and Neutral Mass Spectrometer (*INMS*) (Dong et al., 2015), as well as from the Cosmic Dust Analyzer (*CDA*) (Postberg et al., 2018a). The velocities are compared with estimates from *UVIS* data (Hansen et al., 2006; Tian et al., 2007; Hansen et al., 2008, 2011; Portyankina et al., 2022) and with *INMS* data (Smith et al., 2010; Dong et al., 2011). The objective is to determine how the wall temperature affects the solid fraction and velocity of the water vapour at the vent.

5.1. Wall temperature

The plume flow on Enceladus is expected to have a temperature within a few degrees Kelvin of that of the ice walls (Ingersoll and Pankine, 2010; Nakajima and Ingersoll, 2016). In the experiments with the warm setup, the water vapour, initially in the reservoir near triple point conditions, experienced high heat addition when travelling upwards in the channel (see Fig. 2(a)), reaching highest temperature at the vent. This indicates highly efficient heat transfer, which, as described by Eq. (7), is primarily driven by the wall temperature. This heat transfer inhibits saturated flow and, consequently, phase change processes.

The frozen setup, designed in response to these observations, better reflects the expected conditions of Enceladus' plume. Lower flow temperatures were recorded both within the channel and at the vent (Fig. 2(b)), along with a higher degree of saturation (Fig. 4). A saturated flow is essential for phase change to occur, and phase change is considered the primary mechanism for achieving thermal equilibrium between the flow and the walls, as noted by Nakajima and Ingersoll (2016). Therefore, controlling the setup temperature to better approximate the conditions on Enceladus should be a key focus of future experiments.

5.2. Solid fraction

Cassini *UVIS* and *ISS* observations have been used by Kieffer et al. (2009) and Ingersoll and Ewald (2011) to estimate the solid fraction of the plume, with an inferred ice–vapour mass ratio between 0.1 and 0.7. By fitting the ice grain size distributions measured with *CAPS* and *RPWS*, Dong et al. (2015) derived values of ice grain densities around 20% of the water vapour density measured by the *INMS* data. In comparison, our experimental results show a lower solid fraction of approximately 0.03. These differences arise from the distinct conditions of the experimental setup compared to those of Enceladus' plume, including differences in temperature, scale, and the absence of salts and organic compounds in the liquid water used during the experiments. In this section, we discuss how these parameters may have influenced the solid fractions observed in the experiments.

While the experimental setup has a temperature of 273 K, the crevasse on Enceladus can reach temperatures below 220 K (Spencer et al., 2006; Spencer and Nimmo, 2013; Goguen et al., 2013; Tenishev et al., 2014). As observed in Section 4.3, there is a larger temperature difference between the flow and the wall at the beginning of the experiments, allowing for higher heat transfer towards the walls. As a consequence, the flow becomes supersaturated and nucleation is initiated, increasing the total solid fraction. With lower wall temperatures, we expect to observe higher heat absorption and, consequently, higher nucleation rates.

The second aspect to consider is the model scale. The length of Enceladus crevasses is estimated to be on the order of hundreds of metres to kilometres. In comparison, our model is at least 50 to 1000 times smaller. A longer channel implies a longer time of travel of the icy particles from the water table to the vent and, consequently, a higher possibility for water vapour to deposit onto the existing icy nuclei, promoting their growth and increasing the solid fraction.

Lastly, the use of demineralised water in this study prevented heterogeneous nucleation, as discussed in Section 2. Water-insoluble organic compounds, which are present in the subsurface ocean, may enter the plume's water vapour flow and serve as nucleation sites for ice grains, as suggested by Postberg et al. (2018b) and Khawaja et al. (2019). The concentration of these ice grains, known as Type II grains, was estimated from Cassini CDA measurements around 20%–30% of the total mass of icy particles with sizes of ≈0.2–2 μm in the plume (Postberg et al., 2018a). Future experiments will explore whether the presence of organic compounds in the plume experiment would result in similar percentages of Type II grains and higher values of solid fractions.

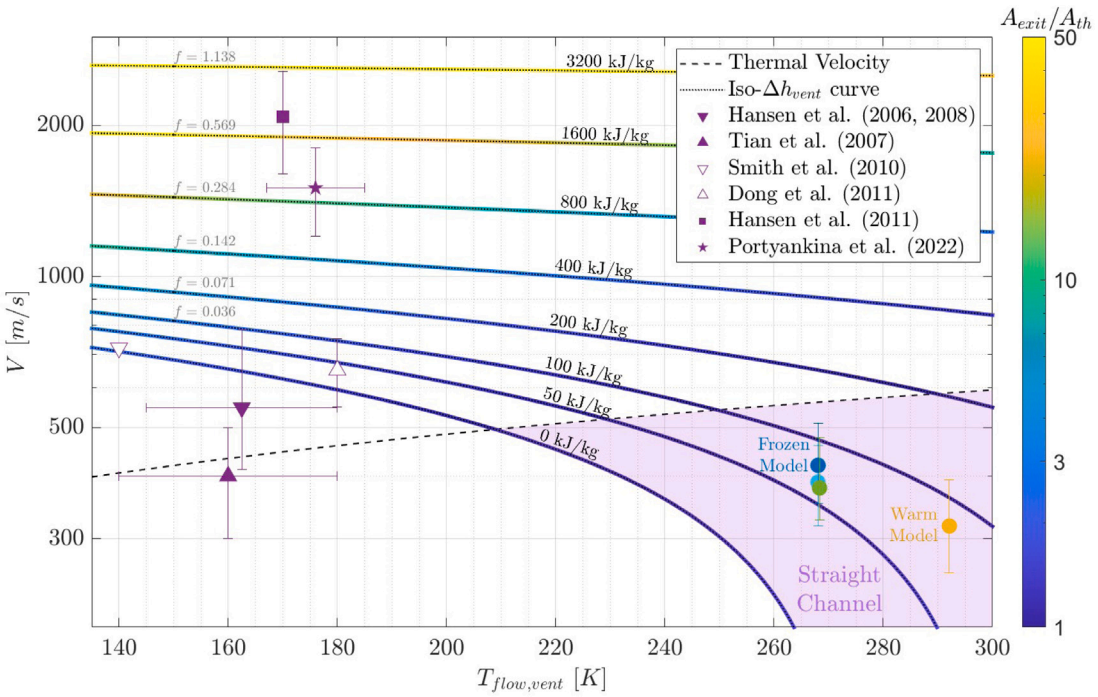

Fig. 9. Experimental plume velocities are the same as in Fig. 8. Results from *UVIS* Cassini observations and *INMS* Cassini observations are reported in purple, with filled and empty markers respectively. The purple-shaded region illustrates the flow temperature–velocity conditions achievable within a straight channel geometry. The minimum values of solid fractions (f), associated with each Δh, have been calculated with Eq. (10) and are indicated in grey on the left-hand side. Yellow–blue gradient lines indicate estimated expansion ratios (A_{exit}/A_{th}) of the channel. (For interpretation of the references to colour in this figure legend, the reader is referred to the web version of this article.)

5.3. Velocity

This section aims to model a correlation between the temperature and the velocity of the water vapour flow. Using the energy conservation equation in Eq. (5), we have calculated the theoretical flow velocity considering various combinations of T_{flow} at the vent, ranging from 260 K and 300 K, and Δh_{vent} equal to 0, 50 and 100 kJ/kg. The reservoir is assumed to be at triple point conditions. This theoretical model, which we refer to as *iso-enthalpy model*, imposes no constraints on the geometry of the channel.

The water vapour velocities associated with the chosen levels of Δh_{vent} are calculated using the iso-enthalpy model and reported in Fig. 8 as black dotted lines. The figure also reports the water vapour velocities obtained from the experiments: 320–500 m/s for the frozen setup and 260–390 m/s for the warm setup, as calculated in Section 3.5.

Both experiment and model agree that lower plume temperatures and higher enthalpy levels correspond to higher water vapour velocities. Moreover, the experimental data points fit within Δh_{vent} values of 50 and 100 kJ/kg. This enthalpy addition (Δh_{vent}) can originate from multiple sources. From the analysis presented in Section 4, we conclude that convection and thermal radiation dominate in the warm setup, while nucleation dominates in the frozen setup.

5.4. From experiments to Cassini observations

In the following paragraphs, we want to examine the possibility of reaching velocities similar to those observed on Enceladus by further cooling the experimental setup. Fig. 9 shows velocities inferred from Cassini observations by several authors. Estimates obtained from *UVIS* by Hansen et al. (2008) and *INMS* observations by Smith et al. (2010) and Dong et al. (2011) are consistent with the estimates of the iso-enthalpy model for Δh_{vent} similar to those observed experimentally. The lower velocities found by Hansen et al. (2006) and Tian et al. (2007) would suggest higher wall temperatures or an under-expanded crevasse (i.e. smaller A_{exit}/A_{th}). However, it should be noted that these studies were published when the plume had just been discovered and few observations were available. Studies by Hansen et al. (2011) and Portyankina et al. (2022) reprocessed these plume observations, obtaining higher water vapour velocities.

The results from Cassini *UVIS* observations exceed the energy levels observed in the experiments. Assuming $T_{flow} \approx T_{wall}$, convective and radiative heat transfers with the crevasse walls can be neglected compared to the heat provided by nucleation. With this assumption, an enthalpy addition of 800–1600 kJ/kg can source from a minimum solid fraction between 0.3 and 0.6, in agreement with Ingersoll and Ewald (2011). Velocities higher than 2000 m/s, estimated by Hansen et al. (2011), require very high Δh and solid fractions (f). Nevertheless, *UVIS* plume observations were taken several kilometres above Enceladus' surface, after the plume experienced additional acceleration through free expansion in vacuum (Yeoh et al., 2017). Therefore, estimates obtained from Hansen et al. (2011) and Portyankina et al. (2022) correspond to an upper limit for the water vapour velocity at the vent.

Several studies, including those of Kieffer et al. (2009) and Ingersoll and Ewald (2011), have reported that the difference between T_{wall} and T_{flow} is typically within 2 K. Applying this assumption to our model, a decrease in wall temperature leads to a corresponding decrease in flow temperature, which, in turn, results in higher flow velocities. However, as shown in Fig. 9, the velocities predicted by the iso-enthalpy model eventually exceed the thermal velocity, v_{th}, indicated by the dashed line and defined by Eq. (11):

$$V_{\mathrm{th}} = \sqrt{\frac{8k_{\mathrm{B}}T}{\pi m}}. \tag{11}$$

where k_{B} is the Boltzmann constant, T is the absolute temperature of the flow, and m is the mass of a single molecule in the flow. When the flow velocity surpasses v_{th}, the efficiency of heat exchange between the flow and the walls is expected to decrease significantly. This is because the average particle velocity increases, reducing the frequency and

duration of collisions between particles and the channel walls. From an experimental point of view, decreasing T_{flow} below 210 K could become unfeasible by solely reducing T_{wall} while keeping a straight channel.

A yellow–blue gradient line has been plotted on top of each iso-enthalpy curve in Fig. 9, indicating how a divergent section of the channel is required to achieve lower flow temperatures. This channel geometry is characterised by a certain exit–throat area ratio (A_{exit}/A_{th}), known as the expansion ratio. While a flow inside a straight channel (expansion ratio 1) can achieve a maximum velocity corresponding to the sound speed and minimum temperatures of 235 K, expansion ratios around 1.5–3 are needed to sustain velocities of 600–1000 m/s and flow temperatures of 140–180 K. This suggests that, by knowing the temperature of the surface around the vent, it may be possible to infer whether the crevasse has a higher expansion ratio (colder surface) or a lower one (warmer surface).

6. Conclusion

We performed plume experiments simulating the thermodynamic conditions found on Enceladus with a water reservoir for the subsurface ocean, a channel for the crevasses, and a vacuum chamber to recreate the low pressures at the surface of the moon. As the pressure decreases, the water reaches boiling conditions and vaporises. Water vapour accelerates through the channel, where flow temperature and pressure are measured, and is ejected in the vacuum chamber.

Two models with straight channels and with different wall temperatures have been tested, allowing us to understand the effect of wall interactions on the flow characteristics. These results have been extended to Enceladus' conditions by considering the effect of longer channel and colder wall temperatures on the flow characteristics. Our conclusions are the following:

1. Convective and radiative heat transfer, highly dependent on the model temperature, play a crucial role in the plume experiments and are the main cause of non-saturated flow in a room temperature model;
2. Saturated flow conditions and visible condensation onto the channel walls of the frozen model have been observed. Nucleation is possible, despite the absence of a geometric throat in the channel, and the solid fraction is estimated around 1.5%–3%;
3. A straight channel configuration was chosen to isolate the thermal effects on the flow velocity. The flow velocity within the channel was observed to be affected by different wall temperatures. The experiments show higher velocities for lower wall temperatures. This aligns with the energy conservation law.
4. A new plume model based on the conservation of energy has been formulated, called the *iso-enthalpy model*. The experiments were conducted at temperatures much higher than the real Enceladus conditions. We argue that the impact of the wall temperatures (T_{wall}) on the flow velocity is greater when T_{wall} is above 210–235 K. Additionally, we emphasise the necessity of an expanding channel to achieve flow temperatures and velocities consistent with Cassini observations. Lastly, we propose a potential link between the surface temperatures observed near the tiger stripes and the expansion ratios of adjacent crevasses, suggesting that warmer surfaces may indicate narrower crevasse vents.

Our research highlights the importance of creating experimental models to better understand processes occurring on Enceladus. This study starts with the model temperature as a key parameter. Future plume experiments will investigate lower model temperatures and evaluate the impact of channel geometry (i.e. different expansion ratios, throat diameters...) on the flow velocity and temperature. Furthermore, higher accuracy measurement techniques are essential to investigate nucleation in the flow, starting from the assessment of the wall temperature and, consequently, heat transfer with the model.

While the present study focuses on Enceladus' plume, the results can be extended to cryovolcanism in general and are therefore applicable to other icy moons such as Europa. Two major missions are currently on their way to the Jovian System to advance our understanding of ocean worlds. NASA's Europa Clipper, launched in 2024, will conduct a detailed reconnaissance of Jupiter's moon Europa, including searches for plumes (Vance et al., 2023). ESA's JUICE (Jupiter Icy Moons Explorer) mission will explore Ganymede, Europa, and Callisto, with particular emphasis on Ganymede (Grasset et al., 2013). ESA's Voyage 2050 program and NASA's Planetary Science Decadal Survey are prioritising further exploration of Enceladus, with potential landers that may attempt to access the subsurface ocean directly. For these future missions, it is essential to understand the physical environments in which robotic systems will have to operate to reach the subsurface ocean. Our experiments can support mission design by providing constraints on crevasse geometry, thermal conditions, and dynamic pressures that may be encountered during descent. The design of mission concepts such as a lander with a melting probe (Konstantinidis et al., 2015) a robot climbing icy crevasses with screws (Ono et al., 2018) or a snake-like autonomous robot designed to navigate icy crevasses (Vaquero et al., 2024), highlight the importance of such preparatory studies.

CRediT authorship contribution statement

Fabrizio Giordano: Writing – original draft, Visualization, Validation, Software, Methodology, Investigation. **Yaël R.A. Bourgeois:** Writing – review & editing, Writing – original draft, Supervision. **Stéphanie M. Cazaux:** Supervision, Methodology. **Ferdinand F.J. Schrijer:** Supervision, Methodology, Conceptualization.

Declaration of competing interest

The authors declare that they have no known competing financial interests or personal relationships that could have appeared to influence the work reported in this paper.

Acknowledgements

The authors would like to thank the NWO PEPSci-II funding scheme for supporting their research on icy moons' exospheres.

Appendix A. Experimental equipment

This section describes the laboratory equipment used for the plume experiments (i.e. the vacuum chamber and pumps), the methods used to measure the pressure, and the precision of the measuring equipment.

A.1. Vacuum chamber and pumps

A section of the *Hypersonic Test Facility Delft (HTFD)* is utilised as vacuum chamber. A schematic of the HTFD is provided by David et al. (2006). The vacuum system uses two Leybold SOGEVAC SV300B pumps to evacuate the vacuum tank. The minimum pressure observed in the vacuum chamber is around 1 mbar. The vacuum pumps evacuate the chamber throughout an experiment to guarantee the lowest pressure possible. Because water vapour is continuously ejected into the vacuum chamber, the typical pressure achieved in the vacuum chamber during a plume experiment is (3.5 ± 0.5) mbar after 10 min from the start of evacuation and does not change significantly over time.

A.2. Pressure measurements

The reservoir pressure was determined based on the water temperature at boiling conditions, employing the Antoine equation:

$$\log_{10} p_{res} = \mathcal{A} - \frac{\mathcal{B}}{\mathcal{C} + T_{water}} \tag{12}$$

where $\mathcal{A}$, $\mathcal{B}$ and $\mathcal{C}$ are gas-related parameters with values of 5.40221, 1838.675, and −31.737 respectively.[2]

Differential pressure sensors have been employed to determine the pressure in other locations along the channel. Each sensor comprises a high-pressure port and a low-pressure port and outputs a voltage signal proportional to the pressure difference between the two ports. The maximum pressure difference detectable ranges between 12.5 and 25 mbar, with an uncertainty of 0.1–0.3 mbar (see Appendix A.3) depending on the specifications of each sensor.

A single differential pressure sensor is used to measure the pressure difference between the reservoir and vacuum chamber and derive the absolute pressure in the latter. Since the low-pressure port of all the differential pressure sensors was exposed to the identical vacuum chamber pressure, it is possible to derive the absolute pressure in each other location.

A.3. Pressure uncertainty

As mentioned before, various differential pressure sensors have been used to monitor the flow conditions inside the reservoir, along the channel and at the vent. Using the accuracy of the various differential pressure sensors (`HCLA12X5EU`, `ELVRL10D1RTINA5F` and `NSCD-JJN005NDUNV` chips) used in our experimental setup, we can derive the global uncertainty on each differential pressure measurement.

$$P_{diff} = \frac{V_{out} - V_{off}}{V_{max} - V_{off}} P_{diff,max} \tag{13}$$

From Eq. (13), we can link the differential pressure measured in mbar to the voltage output of the sensor chip V_{out} and the maximum measurable pressure difference $P_{diff,max}$. The offset voltage when zero differential pressure is applied between the two pressure ports V_{off} and the maximum voltage output value V_{max} are both given by the sensor's manufacturer in its technical datasheet. Propagating the uncertainty of those three voltage parameters with regards to Eq. (13) will yield the total uncertainty on P_{diff}:

$$\sigma^2_{P,diff} = \left(\frac{\partial P_{diff}}{\partial V_{out}}\sigma_{V,out}\right)^2 + \left(\frac{\partial P_{diff}}{\partial V_{off}}\sigma_{V,off}\right)^2 + \left(\frac{\partial P_{diff}}{\partial V_{max}}\sigma_{V,max}\right)^2 \tag{14}$$

The combination of sensors provides an overall uncertainty $\sigma_{P,diff}$ ranging from 0.1 mbar to 0.3 mbar.

A.4. Temperature uncertainty

The uncertainty of T-type thermocouple measurements has been determined by exposing the sensors to an environment with a stable temperature, hence in the absence of gas flows. The average of all the measurements has been considered as the true temperature, while the uncertainty of the measurement has been calculated as 3 times the standard deviation of the measurements, resulting in 0.25 °C.

However, during the plume's experiments, the thermocouples are exposed to the water vapour flow, with temperature constantly varying.

[2] The values of the Antoine equation parameters have been retrieved from the following NIST (National Institute of Standards and Technology) web page, making reference to Bridgeman and Aldrich (1964): https://webbook.nist.gov/cgi/cbook.cgi?ID=C7732185&Mask=4&Type=ANTOINE&Plot=on.

Table 2
Maximum temperature error (ΔT_{real}) for each experiment, assuming 3 different wall temperatures (T_{wall}). All estimates are expressed in degrees Celsius (°C). These errors refer to the experiments reported in Table 1, displayed in Fig. 3. Since experiments 2, 3 and 7 presented unreliable measurements of velocity, the error estimation was not possible.

T_{wall}	15 °C	17.5 °C	20 °C
Exp 1 (warm)	1.84	0.83	0.40
T_{wall}	−5 °C	−2.5 °C	0 °C
Exp 4 (frozen)	0.37	0.87	1.39
Exp 5 (frozen)	0.37	0.97	1.61
Exp 6 (frozen)	0.49	0.89	1.45

Moreover, the thermocouple is subject to thermal radiation coming from the walls. Therefore, the measurements provided by the thermocouples could be different from the real flow temperature. In these conditions, the thermocouple tip is assumed to be in thermal equilibrium with the surrounding environment, meaning that the total contribution of convective and radiative heat transfer should equal zero. We use Eq. (15) to find the real value of the flow temperature (T_{flow}), knowing the temperature measured by the thermocouples (T_{TC}) and assuming different values for the wall temperature (T_{wall}). The product between the view factor and surface area of the channel ($F_{a\to t}A_{wall}$) is assumed approximately equal to the surface area of the thermocouple tip (A_{TC}), in the order of 10^{-5} m^2. The emissivity (ε) was assumed equal to 0.95.

$$F_{a\to t}A_{wall}\varepsilon\sigma(T^4_{TC} - T^4_{wall}) + A_{TC}h_{conv}(T_{TC} - T_{flow}) = 0 \tag{15}$$

The convective heat transfer coefficient h_{conv} is estimated based on several measurements, including the flow velocity (see Appendix C). For experiments where this measurement was unreliable — specifically experiments 2, 3, and 7 in Table 1 — it was not possible to solve Eq. (15). The outcomes, expressed as $\Delta T_{real} = T_{TC} - T_{flow}$, are reported in Table 2 for all the remaining experiments. A T_{wall} between 15 and 20 °C has been assumed for the warm setup, and between −5 and 0 °C for the frozen setup. All the errors are within 2 °C, which is considered the uncertainty for the measurements of flow temperature.

Appendix B. Mach number derivation

A gas flow expanding adiabatically within a channel adheres to the principles of mass, momentum and energy conservation. For a perfect gas, the following equation holds:

$$T_0 = T + \frac{V^2}{2c_p} = T\left(1 + \frac{V^2}{2\frac{\gamma}{\gamma-1}R_{sp}T}\right) = T\left(1 + \frac{\gamma-1}{2}M^2\right) \tag{16}$$

T_0 is the total temperature, equivalent to the flow temperature when its velocity is null. Therefore, knowing the flow static and total temperature, it is possible to derive the Mach number:

$$M = \sqrt{\frac{2}{\gamma-1}\left(\frac{T_0}{T} - 1\right)} \tag{17}$$

If an isentropic flow is assumed, therefore when the process is considered reversible, the Poisson relations hold:

$$\frac{T}{T_0} = \left(\frac{\rho}{\rho_0}\right)^{\gamma-1} = \left(\frac{p}{p_0}\right)^{\frac{\gamma-1}{\gamma}} \tag{18}$$

These can be substituted into Eq. (17) to obtain the Mach number as a function of the flow pressure (Eq. (3)).

Appendix C. Convective heat transfer coefficient h_{conv}

When the system is in static conditions, the measured convective heat transfer coefficient is around 2.5 and 25 W/m^2 K (Kosky et al., 2013), where low values are observed for low pressures in the case of our experiments. In static conditions, we measure the setup temperature with thermocouples inside the channel, as described in Section 2. Thermal equilibrium is quickly reached between the air inside the channel and the surface of the channel itself.

In the presence of flow in the channel, h_{conv} is obtained from the Nusselt number Eq. (19).

$$h_{conv} = \frac{Nu}{d} k \tag{19}$$

The variables in this equation are:

- the characteristic length of the system, in our model the channel diameter d, equal to 5.7 mm;
- the Nusselt number Nu, calculated with Eq. (20), proposed by Nusselt (1931) and valid for short tubes wherein the effect of the entrance region is not negligible. This formula is considered suitable within a range of $10<L/d<400$, where L represents the channel length (245 mm). The model employed in our study has a L/D ratio of approximately 43, aligning with the conditions required by this formula;
- the thermal conductivity of water vapour k, determined with Eq. (21), where c_p is the specific heat capacity of water vapour at constant pressure, dependent on the flow temperature.

The Reynolds number Re is calculated with Eq. (22). The density ρ is obtained from the perfect gas equation. The dynamic viscosity μ, determined with Eq. (23), provided by Crifo (1989) for low vapour temperatures, between 50 K and 300 K. The velocity V is obtained from Mach number measurements at the vent and speed of sound estimate. Here we consider the velocity at the vent to be equal to the bulk velocity through the channel. Since this is an overestimation of the velocity, h_{conv} is overestimated as well. The Prandtl number Pr is considered equal to 0.7 for gases (Rapp, 2017).

$$Nu = 0.036 \cdot Re^{0.8} \cdot Pr^{1/3} \cdot \left(\frac{L}{d}\right)^{-0.054} \tag{20}$$

$$k = \frac{c_p \mu}{Pr} \tag{21}$$

$$Re = \frac{\rho L V}{\mu} \tag{22}$$

$$\mu = 0.925 \times 10^{-5} \left(\frac{T}{300}\right)^{1.1} \tag{23}$$

In the experiments, typical values of Re range around 1500 ± 400 during the initial transitional phase and decrease to 550 ± 150 as the flow approaches a stable state. These Reynolds numbers below 2000 indicate laminar flow. The heat transfer coefficient h_{conv} also decreases throughout the experiment, starting from 25–40 W/m^2 K and stabilising at 15–20 W/m^2 K, with an uncertainty of 8 W/m^2 K.

Appendix D. Mass flow rate $\dot{m}_{flow}$

In this section, the mass flow rate ($\dot{m}_{flow}$) is calculated. First, we apply Eq. (24), derived from the continuity equation. If the flow is choked, $\dot{m}_{flow}$ becomes independent of the vent conditions and Eq. (25) is used. This expression depends on the throat cross-section area A_{th}.

$$\dot{m} = \frac{A P_{res}}{\sqrt{R_{sp} T_{res}}} \sqrt{\frac{2\gamma}{\gamma - 1} \left(\frac{P_{vent}}{P_{res}}\right)^{\frac{2}{\gamma}} \left[1 - \left(\frac{P_{vent}}{P_{res}}\right)^{\frac{\gamma-1}{\gamma}}\right]} \tag{24}$$

$$\dot{m}_{cr} = \frac{A_{th} P_{res}}{\sqrt{R_{sp} T_{res}}} \sqrt{\gamma} \left(\frac{2}{\gamma + 1}\right)^{\frac{\gamma+1}{2(\gamma-1)}} \tag{25}$$

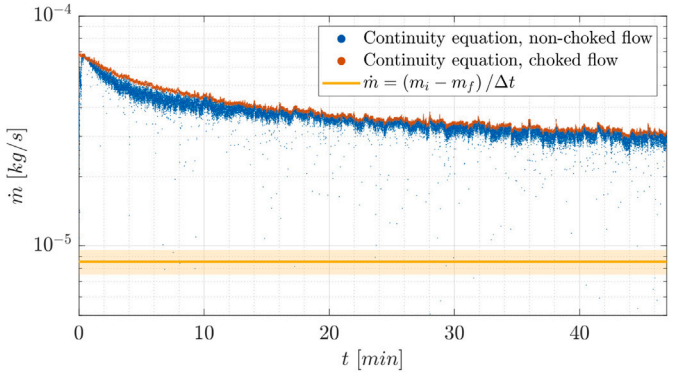

Fig. 10. Mass flow rate of experiment 6 (frozen setup; see Table 1) computed with Eq. (24) (blue), Eq. (25) (orange) and Eq. (26) (yellow). The shaded yellow area represents the uncertainty margin, derived from the weight measurement uncertainty. (For interpretation of the references to colour in this figure legend, the reader is referred to the web version of this article.)

To validate these estimates, the mass of water in the reservoir before and after the experiment has been weighed. Starting from an initial volume of 0.5 L, the reservoir lost on average 0.018–0.023 L of water (initial–final mass, $m_i - m_f$) for an average boiling duration of Δt = 40 min. These measurements translate into an average mass flow rate of 7.5×10^{-6}–10^{-5} kg/s throughout the boiling phase (see Eq. (26)).

$$\dot{m}_{flow} = \frac{m_i - m_f}{\Delta t} \tag{26}$$

One example of a frozen experimental setup is reported in Fig. 10. Similar outcomes are obtained for the warm setup, suggesting that $\dot{m}_{flow}$ is not governed by the wall temperature. We observe that non-choked and choked flow assumptions give approximately the same result. This corroborates the hypothesis of choked flow throughout the experiment. An almost constant mass flow rate is achieved towards the end of the experiment, due to the small change of reservoir and vent conditions with time.

Condensation was observed on the reservoir walls in all experiments, forming large droplets of water. This observation suggests that a portion of the vaporised mass is lost before entering the channel. Consequently, the principles of mass conservation, which underlie Eqs. (24) and (25), no longer hold. The resulting value of $\dot{m}$ is expected to be smaller than estimated with these formulas. These considerations suggest that the mass flow rate is likely around 10^{-5} kg/s under stable flow conditions.

Data availability

Data will be made available on request.

References

Bridgeman, O.C., Aldrich, E.W., 1964. Vapor pressure tables for water. J. Heat Transf. 86, 279–286. http://dx.doi.org/10.1115/1.3687121.

Choukroun, M., Molaro, J.L., Hodyss, R., Marteau, E., Backes, P., Carey, E.M., Dhaouadi, W., Moreland, S., Schulson, E.M., 2020. Strength evolution of ice plume deposit analogs of enceladus and europa. Geophys. Res. Lett. 47, e2020GL088953. http://dx.doi.org/10.1029/2020GL088953.

Crifo, J., 1989. Inferences concerning water vapour viscosity and mean free path at low temperatures. Astron. Astrophys. 223 (OCT (I)), 365, 1989 223, 365.

David, K., Gorham, J., Kim, S., Miller, P., Minkus, C., 2006. Aeronautical Wind Tunnels, Europe and Asia. Library of Congress Washington DC Federal Research Div.

Dong, Y., Hill, T.W., Teolis, B.D., Magee, B.A., Waite, J.H., 2011. The water vapor plumes of enceladus. J. Geophys. Res.: Space Phys. 116, http://dx.doi.org/10.1029/2011ja016693.

Dong, Y., Hill, T.W., Ye, S.Y., 2015. Characteristics of ice grains in the enceladus plume from cassini observations. J. Geophys. Res.: Space Phys. 120, 915–937. http://dx.doi.org/10.1002/2014JA020288, URL https://agupubs.onlinelibrary.wiley.com/doi/abs/10.1002/2014JA020288 arXiv:https://agupubs.onlinelibrary.wiley.com/doi/pdf/10.1002/2014JA020288.

Fifer, L.M., Catling, D.C., Toner, J.D., 2022. Chemical fractionation modeling of plumes indicates a gas-rich, moderately alkaline enceladus ocean. Planet. Sci. J. 3, http://dx.doi.org/10.3847/PSJ/ac7a9f, URL https://iopscience.iop.org/article/10.3847/PSJ/ac7a9f/meta.

Fu, M., Gu, H., Cui, J., Xiao, Z., He, F., Wei, Y., Ren, Z., 2021. On the structure of the enceladus plume. Mon. Not. R. Astron. Soc. 504, 6216–6222. http://dx.doi.org/10.1093/mnras/stab1265.

Gao, P., Kopparla, P., Zhang, X., Ingersoll, A.P., 2016. Aggregate particles in the plumes of enceladus. Icarus 264, 227–238. http://dx.doi.org/10.1016/j.icarus.2015.09.030.

Goguen, J.D., Buratti, B.J., Brown, R.H., Clark, R.N., Nicholson, P.D., Hedman, M.M., Howell, R.R., Sotin, C., Cruikshank, D.P., Baines, K.H., Lawrence, K.J., Spencer, J.R., Blackburn, D.G., 2013. The temperature and width of an active fissure on enceladus measured with cassini vims during the 14 april 2012 south pole flyover. Icarus 226, 1128–1137. http://dx.doi.org/10.1016/j.icarus.2013.07.012, URL https://www.sciencedirect.com/science/article/pii/S0019103513003138.

Goodman, J.C., Collins, G.C., Marshall, J., Pierrehumbert, R.T., 2004. Hydrothermal plume dynamics on europa: Implications for chaos formation. J. Geophys. Res.: Planets 109, http://dx.doi.org/10.1029/2003JE002073.

Grasset, O., Dougherty, M., Coustenis, A., Bunce, E., Erd, C., Titov, D., Blanc, M., Coates, A., Drossart, P., Fletcher, L., Hussmann, H., Jaumann, R., Krupp, N., Lebreton, J.P., Prieto-Ballesteros, O., Tortora, P., Tosi, F., Van Hoolst, T., 2013. Jupiter icy moons explorer (juice): An esa mission to orbit ganymede and to characterise the jupiter system. Planet. Space Sci. 78, 1–21. http://dx.doi.org/10.1016/j.pss.2012.12.002, URL https://www.sciencedirect.com/science/article/pii/S0032063312003777.

Hansen, C.J., Esposito, L.W., Aye, K.M., Colwell, J.E., Hendrix, A.R., Portyankina, G., Shemansky, D., 2017. Investigation of diurnal variability of water vapor in enceladus' plume by the cassini ultraviolet imaging spectrograph. Geophys. Res. Lett. 44, 672–677. http://dx.doi.org/10.1002/2016gl071853.

Hansen, C.J., Esposito, L., Stewart, A.I.F., Colwell, J., Hendrix, A., Pryor, W., Shemansky, D., West, R., 2006. Enceladus' water vapor plume. Science 311, 1422–1425. http://dx.doi.org/10.1126/science.1121254.

Hansen, C.J., Esposito, L.W., Stewart, A.I.F., Meinke, B., Wallis, B., Colwell, J.E., Hendrix, A.R., Larsen, K., Pryor, W., Tian, F., 2008. Water vapour jets inside the plume of gas leaving enceladus. Nature 456, 477–479. http://dx.doi.org/10.1038/nature07542.

Hansen, C., McEwen, A., Ingersoll, A., Terrile, R., 1990. Surface and airborne evidence for plumes and winds on triton. Science 250, 421–424. http://dx.doi.org/10.1126/science.250.4979.421.

Hansen, C.J., Shemansky, D.E., Esposito, L.W., Stewart, A.I.F., Lewis, B.R., Colwell, J.E., Hendrix, A.R., West, R.A., Waite, J.H., Teolis, B., Magee, B.A., 2011. The composition and structure of the enceladus plume. Geophys. Res. Lett. 38, http://dx.doi.org/10.1029/2011gl047415.

Hemingway, D., Iess, L., Tajeddine, R., Tobie, G., 2018. Enceladus and the icy moons of saturn.

Ingersoll, A.P., Ewald, S.P., 2011. Total particulate mass in enceladus plumes and mass of saturn's e ring inferred from cassini ISS images. Icarus 216, 492–506. http://dx.doi.org/10.1016/j.icarus.2011.09.018.

Ingersoll, A.P., Nakajima, M., 2016. Controlled boiling on enceladus, 2. model of the liquid-filled cracks. Icarus 272, 319–326. http://dx.doi.org/10.1016/j.icarus.2015.12.040.

Ingersoll, A.P., Pankine, A.A., 2010. Subsurface heat transfer on enceladus: Conditions under which melting occurs. Icarus 206, 594–607. http://dx.doi.org/10.1016/j.icarus.2009.09.015.

Kempf, S., Horányi, M., Hsu, H., Hill, T., Juhász, A., Smith, H., Schenk, P., Clark, R., Howett, C., Verbiscer, A., et al., 2018. Enceladus and the icy moons of saturn.

Khawaja, N., Postberg, F., Hillier, J., Klenner, F., Kempf, S., Nölle, L., Reviol, R., Zou, Z., Srama, R., 2019. Low-mass nitrogen-, oxygen-bearing, and aromatic compounds in enceladean ice grains. Mon. Not. R. Astron. Soc. 489, 5231–5243. http://dx.doi.org/10.1093/mnras/stz2280.

Kieffer, S.W., Lu, X., McFarquhar, G., Wohletz, K.H., 2009. A redetermination of the ice/vapor ratio of enceladus' plumes: Implications for sublimation and the lack of a liquid water reservoir. Icarus 203, 238–241. http://dx.doi.org/10.1016/j.icarus.2009.05.011.

Kite, E.S., Rubin, A.M., 2016. Sustained eruptions on enceladus explained by turbulent dissipation in tiger stripes. Proc. Natl. Acad. Sci. 113, 3972–3975. http://dx.doi.org/10.1073/pnas.1520507113.

Klenner, F., Fifer, L.M., Journaux, B., Bravenec, A.D., Leal, A.M.M., Vance, S.D., Catling, D.C., 2025. Supercooling, glass formation, and mineral assemblages upon freezing of salty ice grains from enceladus's ocean. Planet. Sci. J. 6, http://dx.doi.org/10.3847/PSJ/adb305, URL https://iopscience.iop.org/article/10.3847/PSJ/adb305/meta.

Konstantinidis, K., Flores Martinez, B., Ohndorf, A., Dykta, P., Bowitz, P., Rudolph, M., Digel, I., Kowalski, J., Voigt, K., Förstner, R., 2015. A lander mission to probe subglacial water on saturn's moon enceladus for life. Acta Astronaut. 106, 63–89. http://dx.doi.org/10.1016/j.actaastro.2014.09.012, URL https://www.sciencedirect.com/science/article/pii/S0094576514003610.

Kosky, P., Balmer, R., Keat, W., Wise, G., 2013. Chapter 12 - mechanical engineering. In: Kosky, P., Balmer, R., Keat, W., Wise, G. (Eds.), Exploring Engineering (Third Edition), third edition ed. Academic Press, Boston, pp. 259–281. http://dx.doi.org/10.1016/B978-0-12-415891-7.00012-1.

Matson, D.L., Castillo-Rogez, J.C., Davies, A.G., Johnson, T.V., 2012. Enceladus: A hypothesis for bringing both heat and chemicals to the surface. Icarus 221, 53–62. http://dx.doi.org/10.1016/j.icarus.2012.05.031.

Mitchell, K.L., Rabinovitch, J., Scamardella, J.C., Cable, M.L., 2024. A proposed model for cryovolcanic activity on enceladus driven by volatile exsolution. J. Geophys. Res.: Planets 129, e2023JE007977. http://dx.doi.org/10.1029/2023JE007977, URL https://agupubs.onlinelibrary.wiley.com/doi/abs/10.1029/2023JE007977 arXiv:https://agupubs.onlinelibrary.wiley.com/doi/pdf/10.1029/2023JE007977, e2023JE007977 2023JE007977.

Nakajima, M., Ingersoll, A.P., 2016. Controlled boiling on enceladus, 1. model of the vapor-driven jets. Icarus 272, 309–318. http://dx.doi.org/10.1016/j.icarus.2016.02.027.

Nusselt, W., 1931. Der wärmeaustausch zwischen wand und wasser im rohr. Forsch. Geb.Ingenieurwesens A 2, 309–313.

Ono, M., Mitchel, K., Parness, A., Carpenter, K., Iacoponi, S., Simonson, E., Curtis, A., Ingham, M., Budney, C., Estlin, T., Parcheta, C., Detry, R., Nash, J., de la Croix, J.P., Kawata, J., Hand, K., 2018. Enceladus Vent Explorer Concept. Springer International Publishing, Cham, pp. 665–717. http://dx.doi.org/10.1007/978-3-319-73845-1_13.

Perry, M., Teolis, B., Hurley, D., Magee, B., Waite, J., Brockwell, T., Perryman, R., McNutt, R., 2015. Cassini INMS measurements of enceladus plume density. Icarus 257, 139–162. http://dx.doi.org/10.1016/j.icarus.2015.04.037.

Porco, C.C., Helfenstein, P., Thomas, P.C., Ingersoll, A.P., Wisdom, J., West, R., Neukum, G., Denk, T., Wagner, R., Roatsch, T., Kieffer, S., Turtle, E., McEwen, A., Johnson, T.V., Rathbun, J., Veverka, J., Wilson, D., Perry, J., Spitale, J., Brahic, A., Burns, J.A., DelGenio, A.D., Dones, L., Murray, C.D., Squyres, S., 2006. Cassini observes the active south pole of enceladus. Science 311, 1393–1401. http://dx.doi.org/10.1126/science.1123013.

Portyankina, G., Esposito, L.W., Aye, K.M., Hansen, C.J., Ali, A., 2022. Modeling the complete set of cassini's UVIS occultation observations of enceladus' plume. Icarus 383, 114918. http://dx.doi.org/10.1016/j.icarus.2022.114918.

Postberg, F., Clark, R.N., Hansen, C.J., Coates, A.J., Dalle Ore, C.M., Scipioni, F., Hedman, M.M., Waite, J.H., 2018a. Plume and surface composition of enceladus. In: Enceladus the Icy Moons Saturn. Vol. 129.

Postberg, F., Kempf, S., Schmidt, J., Brilliantov, N., Beinsen, A., Abel, B., Buck, U., Srama, R., 2009. Sodium salts in e-ring ice grains from an ocean below the surface of enceladus. Nature 459, 1098–1101. http://dx.doi.org/10.1038/nature08046.

Postberg, F., Khawaja, N., Abel, B., Choblet, G., Glein, C.R., Gudipati, M.S., Henderson, B.L., Hsu, H.W., Kempf, S., Klenner, F., Moragas-Klostermeyer, G., Magee, B., Nölle, L., Perry, M., Reviol, R., Schmidt, J., Srama, R., Stolz, F., Tobie, G., Trieloff, M., Waite, J.H., 2018b. Macromolecular organic compounds from the depths of enceladus. Nature 558, 564–568. http://dx.doi.org/10.1038/s41586-018-0246-4.

Rapp, B.E., 2017. Chapter 9-fluids. Microfluid.: Model. Mech. Math. 263.

Schmidt, J., Brilliantov, N., Spahn, F., Kempf, S., 2008. Slow dust in enceladus' plume from condensation and wall collisions in tiger stripe fractures. Nature 451, 685–688. http://dx.doi.org/10.1038/nature06491.

Smith, H.T., Johnson, R.E., Perry, M.E., Mitchell, D.G., McNutt, R.L., Young, D.T., 2010. Enceladus plume variability and the neutral gas densities in saturn's magnetosphere. J. Geophys. Res.: Space Phys. 115, http://dx.doi.org/10.1029/2009ja015184.

Soderblom, L.A., Kieffer, S., Becker, T., Brown, R.H., Cook, A., Hansen, C., Johnson, T., Kirk, R.L., Shoemaker, E., 1990. Triton's geyser-like plumes: Discovery and basic characterization. Science 250, 410–415. http://dx.doi.org/10.1126/science.250.4979.410.

Spencer, J.R., Nimmo, F., 2013. Enceladus: An active ice world in the saturn system. Annu. Rev. Earth Planet. Sci. 41, 693–717. http://dx.doi.org/10.1146/annurev-earth-050212-124025.

Spencer, J.R., Pearl, J.C., Segura, M., Flasar, F.M., Mamoutkine, A., Romani, P., Buratti, B.J., Hendrix, A.R., Spilker, L.J., Lopes, R.M.C., 2006. Cassini encounters enceladus: Background and the discovery of a south polar hot spot. Science 311, 1401–1405. http://dx.doi.org/10.1126/science.1121661.

Stull, D.R., 1947. Vapor pressure of pure substances. Org. Inorg. Compd. Ind. Eng. Chem. 39, 517–540. http://dx.doi.org/10.1021/ie50448a022.

Tenishev, V., Öztürk, D.C.S., Combi, M.R., Rubin, M., Waite, J.H., Perry, M., 2014. Effect of the tiger stripes on the water vapor distribution in enceladus' exosphere. J. Geophys. Res.: Planets 119, 2658–2667. http://dx.doi.org/10.1002/2014JE004700.

Tian, F., Stewart, A., Toon, O., Larsen, K., Esposito, L., 2007. Monte carlo simulations of the water vapor plumes on enceladus. Icarus 188, 154–161. http://dx.doi.org/10.1016/j.icarus.2006.11.010.

Tucker, O.J., Combi, M.R., Tenishev, V.M., 2015. 2D models of gas flow and ice grain acceleration in enceladus' vents using dsmc methods. Icarus 257, 362–376. http://dx.doi.org/10.1016/j.icarus.2015.05.012.

van der Hijden, N.J., Giordano, F., Scholts, S.O.O., Sklavenitis, S., Bründl, T.M., Bourgeois, Y.R., Schrijer, F.F., Cazaux, S.M., 2024. Linking enceladus' plume characteristics to the crevasse properties. Icarus 417, 116114. http://dx.doi.org/10.1016/j.icarus.2024.116114.

Vance, S.D., Craft, K.L., Shock, E., Schmidt, B.E., Lunine, J., Hand, K.P., McKinnon, W.B., Spiers, E.M., Chivers, C., Lawrence, J.D., Wolfenbarger, N., Leonard, E.J., Robinson, K.J., Styczinski, M.J., Persaud, D.M., Steinbrügge, G., Zolotov, M.Y., Quick, L.C., Scully, J.E.C., Becker, T.M., Howell, S.M., Clark, R.N., Dombard, A.J., Glein, C.R., Mousis, O., Sephton, M.A., Castillo-Rogez, J., Nimmo, F., McEwen, A.S., Gudipati, M.S., Insoo, J., Xianzhe, J., Frank, P., Soderlund, K.M., Elder, C.M., 2023. Investigating Europa's habitability with the Europa Clipper. Space Science Reviews (ISSN: 0038-6308) 219 (8), http://dx.doi.org/10.1007/s11214-023-01025-2.

Vaquero, T.S., Daddi, G., Thakker, R., Paton, M., Jasour, A., Strub, M.P., Swan, R.M., Royce, R., Gildner, M., Tosi, P., Veismann, M., Gavrilov, P., Marteau, E., Bowkett, J., de Mola Lemus, D.L., Nakka, Y., Hockman, B., Orekhov, A., Hasseler, T.D., Leake, C., Nuernberger, B., Proença, P., Reid, W., Talbot, W., Georgiev, N., Pailevanian, T., Archanian, A., Ambrose, E., Jasper, J., Etheredge, R., Roman, C., Levine, D., Otsu, K., Yearicks, S., Melikyan, H., Rieber, R.R., Carpenter, K., Nash, J., Jain, A., Shiraishi, L., Robinson, M., Travers, M., Choset, H., Burdick, J., Gardner, A., Cable, M., Ingham, M., Ono, M., 2024. Eels: Autonomous snake-like robot with task and motion planning capabilities for ice world exploration. Sci. Robot. 9, eadh8332. http://dx.doi.org/10.1126/scirobotics.adh8332, URL https://www.science.org/doi/abs/10.1126/scirobotics.adh8332 arXiv:https://www.science.org/doi/pdf/10.1126/scirobotics.adh8332.

Viisanen, Y., Kulmala, M., Laaksonen, A., 1997. Experiments on gas–liquid nucleation of sulfuric acid and water. J. Chem. Phys. 107, 920–926. http://dx.doi.org/10.1063/1.474445.

Vorburger, A., Wurz, P., 2021. Modeling of possible plume mechanisms on europa. J. Geophys. Res.: Space Phys. 126, e2021JA029690. http://dx.doi.org/10.1029/2021JA029690.

Yeoh, S.K., Chapman, T.A., Goldstein, D.B., Varghese, P.L., Trafton, L.M., 2015. On understanding the physics of the enceladus south polar plume via numerical simulation. Icarus 253, 205–222. http://dx.doi.org/10.1016/j.icarus.2015.02.020.

Yeoh, S.K., Li, Z., Goldstein, D.B., Varghese, P.L., Levin, D.A., Trafton, L.M., 2017. Constraining the enceladus plume using numerical simulation and cassini data. Icarus 281, 357–378. http://dx.doi.org/10.1016/j.icarus.2016.08.028.